FULL PAPER

Magnetic Resonance in Medicine 00:00–00 (2015)

Multi-Atlas and Label Fusion Approach for Patient-Specific MRI Based Skull Estimation

Angel Torrado-Carvajal,[1,2]* Joaquin L. Herraiz,[2,3] Juan A. Hernandez-Tamames,[1,2] Raul San Jose-Estepar,[2,4] Yigitcan Eryaman,[2,3,5] Yves Rozenholc,[6,7] Elfar Adalsteinsson,[2,8,9,10] Lawrence L. Wald,[5,9] and Norberto Malpica[1,2]

Purpose: MRI-based skull segmentation is a useful procedure for many imaging applications. This study describes a methodology for automatic segmentation of the complete skull from a single T1-weighted volume.

Methods: The skull is estimated using a multi-atlas segmentation approach. Using a whole head computed tomography (CT) scan database, the skull in a new MRI volume is detected by nonrigid image registration of the volume to every CT, and combination of the individual segmentations by label-fusion. We have compared Majority Voting, Simultaneous Truth and Performance Level Estimation (STAPLE), Shape Based Averaging (SBA), and the Selective and Iterative Method for Performance Level Estimation (SIMPLE) algorithms.

Results: The pipeline has been evaluated quantitatively using images from the Retrospective Image Registration Evaluation database (reaching an overlap of $72.46 \pm 6.99\%$), a clinical CT-MR dataset (maximum overlap of $78.31 \pm 6.97\%$), and a whole head CT-MRI pair (maximum overlap 78.68%). A qualitative evaluation has also been performed on MRI acquisition of volunteers.

Conclusion: It is possible to automatically segment the complete skull from MRI data using a multi-atlas and label fusion approach. This will allow the creation of complete MRI-based tissue models that can be used in electromagnetic dosimetry applications and attenuation correction in PET/MR. **Magn Reson Med 000:000–000, 2015. © 2015 Wiley Periodicals, Inc.**

Key words: atlas-based; label fusion; MRI; skull segmentation; tissue models

INTRODUCTION

Skull segmentation from MRI data is receiving a lot of attention, as there are many applications in which a precise delineation of the skull is needed, in addition to soft tissues. Accurate construction of patient-specific tissue models for dosimetry applications in electromagnetics (EM) (1,2), medical radiation physics (3), or the use of tissue information for attenuation correction in positron emission tomography (PET)/MR (4–6) are three of the most important examples. Treating bone as soft tissue or ignoring it in those applications is known to cause a distorted and biased distribution in the final estimation maps: B1+ field, specific absorption rate (SAR), standardized uptake value (SUV) distribution.

Most common approaches to patient-specific model creation are based on a combination of MRI and computed tomography (CT) images of the subject (7). Figure 1 shows how the MRI allows to better differentiate between soft tissues and to establish their boundaries, while CT provides the bone tissue information.

The use of only MRI instead of MRI+CT has the advantage of reducing radiation dose to subjects, decreasing costs and acquisition time, while allowing detailed information of soft tissues. It will also allow more complete (bigger field of view with respect to CT) and repeated skull imaging of the patient. Nevertheless, MRI-based bone segmentation, specifically automatic segmentation of the skull, is a challenging task. On one hand, bone tissue and air both present low signal intensity on MR images, making it difficult to accurately delimit the bone boundaries. On the other hand, the high complexity of the skull anatomy, its fuzzy boundaries and missing edge features hinders the application of general-purpose segmentation methods.

Background

Several skull segmentation or estimation approaches from MRI images have been presented in the recent literature, based on image postprocessing techniques or on the acquisition of multiple or specific MRI sequences.

[1]Medical Image Analysis and Biometry Lab, Universidad Rey Juan Carlos, Mostoles, Madrid, Spain.

[2]Madrid-MIT M+Vision Consortium, Madrid, Spain.

[3]Research Laboratory of Electronics, Massachusetts Institute of Technology, Cambridge, Massachusetts, USA.

[4]Department of Radiology, Brigham and Women's Hospital, Boston, Massachusetts, USA.

[5]A.A. Martinos Center for Biomedical Imaging, Department of Radiology, Massachusetts General Hospital, Charlestown, Massachusetts, USA.

[6]MAP5, CNRS UMR 8145, University Paris Descartes, Paris, France.

[7]INRIA Saclay – Ile de France – SELECT, Paris, France.

[8]Department of Electrical Engineering and Computer Science, Massachusetts Institute of Technology, Cambridge, Massachusetts, USA.

[9]Harvard-MIT Health Sciences and Technology, Massachusetts Institute of Technology, Cambridge, Massachusetts, USA.

[10]Institute of Medical Engineering and Science, Massachusetts Institute of Technology, Cambridge, Massachusetts, USA.

Grant sponsor: Comunidad de Madrid; Grant sponsor: Madrid-MIT M+Vision Consortium.

*Correspondence to: Angel Torrado-Carvajal, M.Sc. in Biomedical Engineering, Medical Image Analysis and Biometry Lab, Universidad Rey Juan Carlos, Mostoles, Madrid, Spain.
E-mail: angel.torrado@urjc.es

Received 17 November 2014; revised 23 March 2015; accepted 25 March 2015

DOI 10.1002/mrm.25737
Published online 00 Month 2015 in Wiley Online Library (wileyonlinelibrary.com).

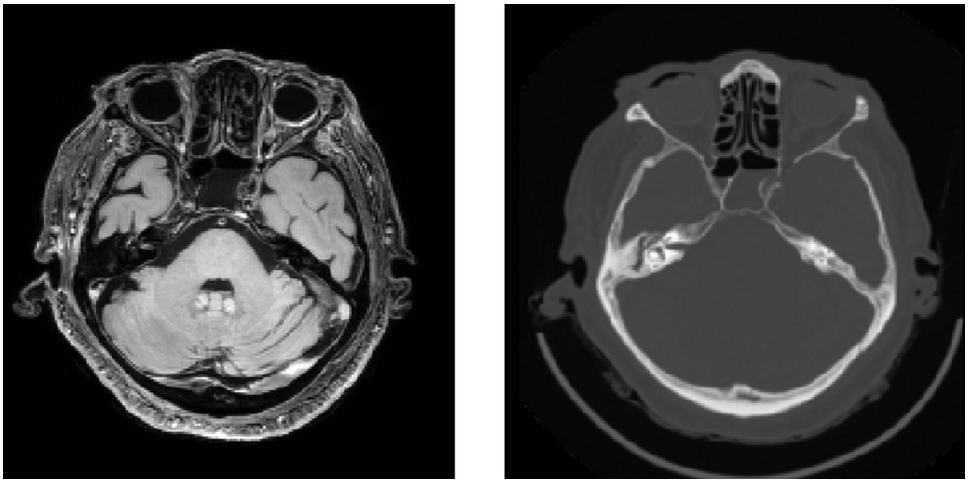

FIG. 1. T1-weighted MR image (left) and CT image (right) of the same subject. We can appreciate how soft tissues can be differentiated in the MRI and not in the CT using low dose X-Ray, while air (lowest signal) and bone (highest signal) can be distinguished in the CT, but not in the MRI (both provide a low signal).

Image Postprocessing

Mathematical morphology analyses and processes geometrical structures in a binary image by using a structuring element; the operations over the structuring element include intersection, union, inclusion, and complementation. These morphological operators can be used on graphs, surface meshes, solids, and many other spatial structures.

Several approaches have also used deformable models based on an initial surface of the skull, deformed subject to artificial forces derived from the desired features of the segmentation. The strength of these models arises from their ability to include high-level information with low-level local features.

In Akahn et al (8), the authors use T1-weighted and proton density images to segment the skull and other tissues with a hybrid algorithm that uses snakes, region growing, morphological operations, and thresholding. The method described in Dogdas et al (9) finds the inner and outer skull boundaries in T1-weighted images using thresholding and morphological operations, and mask the results with the scalp and brain segmentations to ensure closed and nonintersecting skull boundaries.

Rifai et al (10) proposed a three-dimensional (3D) method for segmenting bone regions in MRI volumes using deformable models and taking the partial volume effect into account. In Wang et al (11) the authors proposed the use of a CT database to create a reliable shape model used to locate the skull shape in MRI.

Most of these works are focused on the upper part of the head, as they only have to deal with tissues surrounding the brain. However, the inclusion of the jaw in the complete head models complicates the application of these methods due to its different signal in MRI. Only the methods based on deformable models have dealt with the complete skull segmentation approach.

Multiple MRI Sequences

The detection of signals from tissues and tissue components with very short T2s is now possible due to the development and implementation of the ultrashort echo time (UTE) sequences (12). These sequences allow detecting signal from previously unobservable tissues such as cortical bone, tendons, ligaments, and menisci. However, classification of the skull in MRI has often been a by-product of classification techniques designed to categorize brain tissue. Several approaches are now focused on these techniques, but need multiple samples for each voxel to determine the corresponding output.

Keereman et al (13) proposed the use of the transverse relaxation rate derived from UTE images to classify the voxels into skull, soft tissue, and air. In Berker et al (14), the authors used UTE triple-echo (UTILE) MRI sequence for bone detection and gradient echoes for Dixon water and fat separation.

These methods show a good accuracy for the skull segmentation task, but they do not guarantee continuous bounding contours which can be a problem for meshing and EM simulation. Additionally, they show limited accuracy of bone segmentation in the interface between bone and air. As each radial projection passes through the center of k-space, the signals are indeed heavily averaged resulting in a considerable reduction of motion artifacts. However, the radial approach translates into an increased blurring, hindering edge detection.

In Belardinelli et al (15), the authors used an approach based on neural networks to segment the skull and the brain from successive T1-weighted 2D images. Hsu et al (16) proposed a method consisting of acquiring T1-weighted, T2-weighted, two echoes from a UTE sequence, and fat and water images using a Dixon method, to classify tissues using fuzzy c-means clustering.

The use of these approaches increase the overall acquisition time. The oversampling of the center of k-space in radial imaging for the UTE sequence makes the acquisition last $\frac{\pi}{2}$ times longer than a conventional Cartesian acquisition for the same matrix size. The use of several MRI sequences increase even more the complete acquisition time, depending on the nature and the number of sequences to acquire. For this reason, skull segmentation using a unique T1-weighted MRI sequence is desirable, as they are routinely acquired in clinical settings.

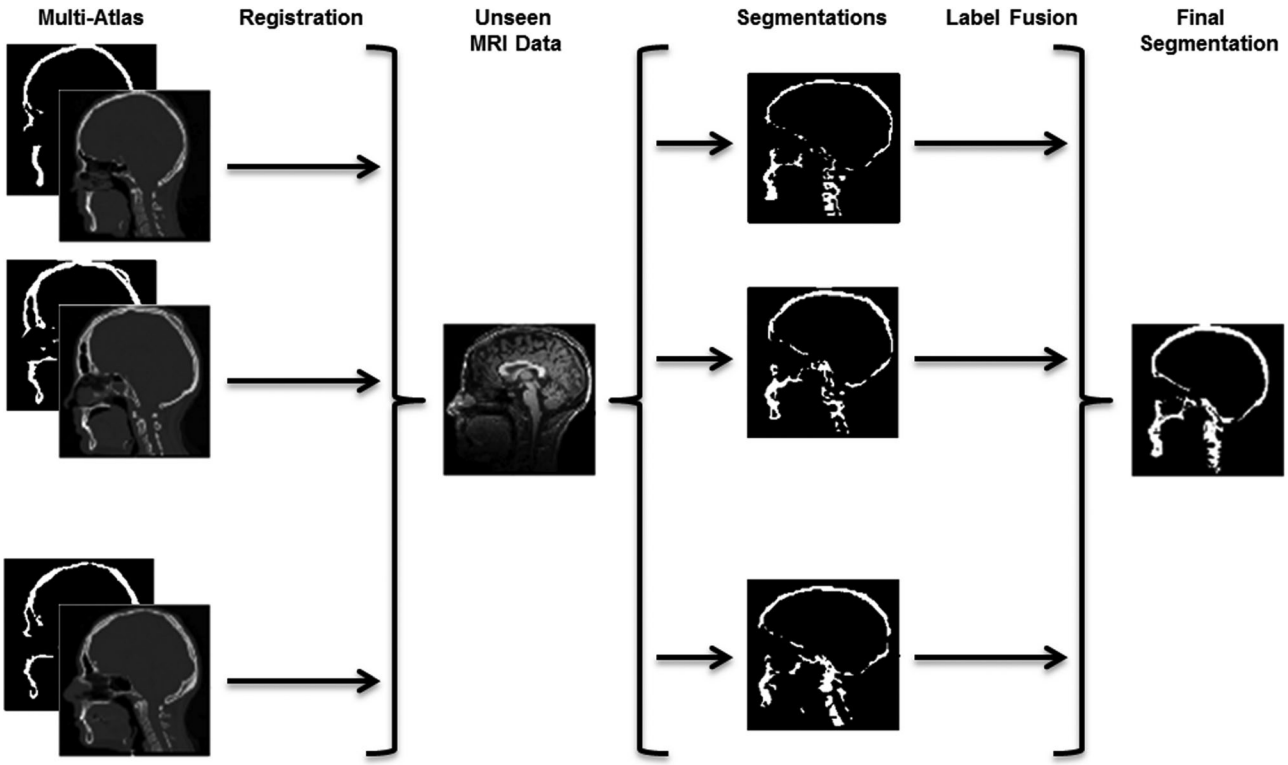

FIG. 2. Skull estimation pipeline based only on patient-specific MRI. The different CT volumes V_n and their corresponding segmentations L_n of the multi-atlas A are registered (affine and non-rigid) to the new MRI data V_{MRI}. Then, label fusion techniques are applied to obtain an estimation of the patient-specific skull L_{MRI}.

Contribution

In this work, we propose a new approach for complete skull estimation based only on T1-weighted images of the human head. This work is the development and assessment of the idea presented in Torrado-Carvajal et al (17), as part of a complete pipeline for tissue segmentation based on MRI only (18).

We use the patient's MRI T1-weighted images and register the volumes from a multi-atlas CT database. The final segmentation is then statistically estimated from the individual segmentations. This approach deals with the limitations of the previous approaches presented above, and offers a general approach to accurately segment the skull.

We have compared the results provided by four different label fusion methods: majority voting (MV) (19), simultaneous truth and performance level estimation (STAPLE) (20), shape-based averaging (SBA) (21), and selective and iterative method for performance level estimation (SIMPLE) (22).

In this study, we demonstrate that a statistical combination of the multi-atlas data provides highly accurate segmentations. The study is structured as follows: the implementation of the skull segmentation algorithm is detailed, including the description of the multi-atlas CT database, the registration process of the multi-atlas to the patient-specific MRI standard space, a description of the different label fusion techniques used in this work and an introduction of the MRI data sets used to obtain the quantitative measures and the experimental results in Section 3; Section 4 establishes a discussion about our work including its limitations; in Section 5 we draw conclusions and comment on future work.

METHODS

An overview of our multi-Atlas and label fusion skull segmentation pipeline is shown in Figure 2. In this multi-atlas based segmentation approach, the unknown ground truth segmentation mask L_{GT} of the MRI volume V_{MRI} is estimated as L_{MRI} by registration of a set of N CT volumes V_n and propagating their corresponding segmentations L_n. The major steps of the pipeline are: (i) *Multi-Atlas CT database*. Generation of the multi-atlas CT database $A_n = (V_n, L_n)$, where A_n denotes an element in the atlas, V_n is a CT volume, and L_n its corresponding segmentation label map. (ii) *CT-MR intermodality registration*. Registration of each atlas volume V_n to the patient-specific target volume V_{MRI}, and propagation of each atlas label L_n to the target volume standard space, obtaining a new L' label set containing N label maps L'_n. (iii) *Label fusion*. Combination of the propagated segmentations L'_n to create an estimation L_{MRI} of the ground truth L_{GT}.

Step 1: Multi-Atlas CT Database

We use the CT volumes V_n from the whole head CT-scan database for craniofacial reconstruction developed by Tilotta et al (23). The images were acquired from healthy volunteers using whole head Somatom Sensation 16 CT

scanners (Siemens, Erlangen) at the Ouest Parisien (Val d'Or, Saint-Cloud, France) Medical Imaging Center. Subjects were positioned supine. For the current work, we have used a subset of the database, consisting of 19 subjects with ages ranging from 20 to 65 years old.

The segmentation of the CT volumes L_n is performed by thresholding of the CT data. The Hounsfield scale allows easily differentiating bone from the rest of the tissues. Additionally, an expert radiologist corrected the segmentations to delete segmentation errors due to dental restorations artifacts. These facts ensure that the segmentations are close to the actual ground truth, making the possible intra-rater reliability of the CT segmentation close to zero.

Step 2: CT-MRI Intermodality Registration

Every CT volume V_n from the atlas A is registered to the MRI volume V_{MRI} and each atlas segmentation L_n is propagated to the unseen data standard space (MRI space). To do so, we first need to pre-align the atlas volumes with the MRI volume using an affine registration, and then refine the registration using a nonrigid transformation.

Mutual Information

As we are dealing with intersubject CT-MR intermodality registration, we need a measure of the mutual dependence between the images. Mutual information (MI) is a distance measure described in the field of information theory by Collignon et al (24) and Viola and Wells (25). MI is a measure of the mutual dependence of two random variables computed from the gray level joint density of the volumes. The MI of two volumes V_A and V_B can be defined as:

$$MI(V_A, V_B) = \sum_{a \in A} \sum_{b \in B} \rho(a,b) log \frac{\rho(a,b)}{\rho(a)\rho(b)} \quad [1]$$

where $\rho(a,b)$ is the joint density function of V_A and V_B, and $\rho(a)\ \ \rho(b)$ are the marginal probability distribution functions of V_A and V_B, respectively. MI is considered as one of the most accurate and robust distance metrics used in registration (26,27).

Affine Registration

As the new MRI volume V_{MRI} is acquired in a different modality than the volumes in the atlas A, the affine registration step transforms the CT volumes V_n in the atlas to roughly align to V_{MRI} and prepare them for the nonrigid registration step. This registration can be performed by directly registering each CT volume V_n to the MRI volume V_{MRI}, obtaining the corresponding transformation matrix T_n^A. However, an efficient way to make the pre-alignment of the atlas volumes can be performed as follows:

1. Create an affine registered atlas, $A^{A_{CT}}$, where each CT volume $V_m \ \forall \ m = 2, \ldots, N$ is affine registered to the volume V_1 used as reference. In this case $A_n^{A_{CT}} = \left(V_n^{A_{CT}}, T_n^{A_{CT}}\right)$, where $V_n^{A_{CT}}$ is the volume V_n transformed to the V_1 space, and $T_n^{A_{CT}}$ the corresponding transformation matrix used to obtain this correspondence.
2. Affinely register the MRI volume V_{MRI} to the CT reference volume V_1, obtaining the corresponding transformation matrix $T_{MRI}^{A_{CT}}$.
3. Concatenate the inverse transformation matrix $T_{CT}^{A_{MRI}^{-1}}$ with each individual transformation matrix $T_n^{A_{CT}}$ of each atlas volume $V_n^{A_{CT}}$ producing a final transformation matrix $T_n^{A'}$ which is applied to obtain the transformed volumes $V_n^{A'}$.

The transformation matrices T_n^A and the transformation matrices $T_n^{A'}$ may differ slightly; however, they seem to be good enough to serve as initialization for the nonrigid registration step. This efficient pre-alignment reduces in a factor of N the computational time for the affine registration.

Nonrigid Registration

Once the Atlas volumes V_n are pre-aligned with the MRI volume V_{MRI}, we need to refine the registration to maximize the similarity between each volume $V_n^{A'}$ and the volume V_{MRI}. This step can be performed by directly nonrigid registering each CT volume $V_n^{A'}$ to V_{MRI}. In this step we obtain the corresponding transformation $T_n^{D'}$ for each volume in the atlas $A_n^{A_{CT}}$.

Label Map Propagation

The transformation matrices $T_n^{A'}$ and the transformations $T_n^{D'}$ are then concatenated to obtain the complete transformations $T_n^{'}$. These $T_n^{'}$ are used to directly propagate the segmentation label maps L_n to the MRI standard space as $L_n^{'}$.

Step 3: Label Fusion

Once we have registered the N CT volumes V_n and propagated their corresponding segmentations L_n to the MRI standard space V_{MRI} of the new data, the final patient-specific skull segmentation L_{MRI} is estimated as a combination of all the segmentations, $L_n^{'}$, by using label fusion techniques. Label fusion exploits multi-atlas segmentation as an inference algorithm based on a nonparametric probabilistic model (28); thus, this technique decides how to fuse the information from several registered label maps. In this work, we have compared four label fusion procedures: MV (19), STAPLE (20), SBA (21), and SIMPLE (22) algorithms. Details of every method can be found in the online Supporting Information.

DATA SETS

To evaluate the complete segmentation pipeline, and the result of applying the different label fusion methods, we need T1 input volumes with a known ground truth. We have used data from different sources.

RIRE

The Retrospective Image Registration Evaluation (RIRE) project was designed to compare retrospective CT-MR and PET-MR registration techniques (29). The database

contains several intra-patient brain CT, MR, and PET volumes acquired at Vanderbilt University Medical Center. These datasets are now available as open-access data (30). Volumes present several voxel sizes in x and y, and a space between slices of 3 or 4 mm.

As the RIRE project aims at assessing different registration methods, images from the dataset are not aligned (the "truth" transforms were defined using a prospective, marker-based technique, but they remain unpublished). Thus, we have used the same registration methods as in our pipeline to register the CT images to their corresponding MR images.

Clinical CT-MRI Pairs

A retrospective dataset consisting of six patients of Ruber International Hospital in Madrid that had undergone neurosurgery were analyzed. Every patient had an MR and a CT volume. MR images had been acquired on a General Electric Signa HDxt 3.0 Tesla (T) MR scanner using the body coil for excitation and an eight-channel quadrature brain coil for reception. Subjects were positioned supine. Imaging was performed using an isotropic 3DT1w SPGR sequence with a repetition time (TR) = 10.8 ms, TE = 4.2 ms, inversion time (TI) = 0 ms, number of excitations (NEX) = 1, acquisition matrix = 256 × 192, resolution = 1 mm × 1 mm × 1 mm, flip angle = 20.

Low-dose CT images were acquired on a General Electric Lightspeed VCT scanner with matrix = 512 × 512, resolution = 0.56 × 0.56 mm, slice thickness = 1.25 mm, PITCH = 0.53 mm, acquisition angle = 0°, voltage = 120 kV, radiation intensity = 200 mA. The examination is performed with the subject in the dorsal decubitus position.

Head MR Images

The present study was approved by the Instituto Carlos III Ethics Board and informed consent was obtained from all subjects before recruitment. Our dataset includes a total of 12 healthy subjects (4 males/8 females) aged 22–57 participating in this study. We also acquired an MRI volume for one of the subjects in the original CT database.

Images of the head were acquired on a General Electric Signa HDxt 3.0T MR scanner using the body coil for excitation and an eight-channel quadrature brain coil for reception. Subjects were positioned supine. Imaging was performed using an isotropic 3DT1w SPGR sequence with a TR = 10.024 ms, TE = 4.56 ms, TI = 600 ms, NEX = 1, acquisition matrix = 288 × 288, resolution = 1 × 1 × 1 mm, flip angle = 12. All image datasets were preprocessed using 3D Slicer built-in modules. The preprocessing step included MRI bias correction (N4 ITK MRI bias correction).

IMPLEMENTATION DETAILS

The skull segmentation pipeline has been implemented as an extension of 3D Slicer (31), as shown in Figure 3. The 3D Slicer is a free and open source software platform for visualization and image analysis of medical data. The 3D Slicer platform leverages the benefits of different open-source libraries such as the Insight Registration and Segmentation Toolkit (ITK) and the Visualization Toolkit (VTK), and allows rapid prototyping and development of medical imaging tools and applications (32,33).

The registration steps of the pipeline are performed with the built-in registration module (BRAINSFit) (34), using Mattes Mutual Information with a b-spline transformation model. This step allows registering the atlas dataset to the new volume to apply on of the different label fusion techniques.

MV and SIMPLE have been implemented as embedded Python code in the extension, while we have used the open source implementations of STAPLE –available as part of the Computational Radiology Kit (http://www.nitrc.org/projects/cmtk/) (CRKit)– and SBA –available as part of the Computational Morphometry Toolkit (http://nitrc.org/projects/cmtk/) (CMTK) – for this first development. All the experiments presented in this study were performed over Ubuntu Precise (12.04.3 LTS) on an Intel(R) Core(TM) i7-2600 CPU @ 3.40GHz with 8GB RAM.

RESULTS

In this section, we describe the main quantitative and qualitative results obtained on the datasets.

Quantitative Results

We have used the RIRE and the clinical CT-MRI pairs as input datasets to quantitatively evaluate the performance of the skull estimation pipeline. These datasets contained 16 and 6 subjects, respectively, where we measured the overlap between the ground truth and our estimation by using the Dice coefficient (35).

The Dice coefficient quantifies the similarity between regions by quantifying the spatial overlap. The Dice coefficient is computed as shown in Eq. [2]. Compared with Euclidean distance, the Dice coefficient gives more weight to voxels where the two images classification agree, and retains sensitivity in more heterogeneous data sets by giving less weight to outliers. Its values range between 0 (no overlap) and 1 (perfect agreement).

$$D = \frac{2(A \cap B)}{(A \cap B) + (A \cup B)} \quad [2]$$

Figure 4A shows the performance of the different label fusion methods on the RIRE dataset. The Dice coefficient between the ground truth and the automated segmentation presents an overlap of $37.66 \pm 7.54\%$ for MV and SIMPLE, $71.79 \pm 7.28\%$ for STAPLE, and $72.46 \pm 6.99\%$ for SBA. Due to the low resolution in the z axis of the volumes in the RIRE database, the registration of some of the volumes in the database is not correct. Majority voting and SIMPLE are not able to discard these results, thus providing very bad segmentation results. STAPLE and SBA iteratively select the better registrations in the database, thus allowing to obtain a good final segmentation.

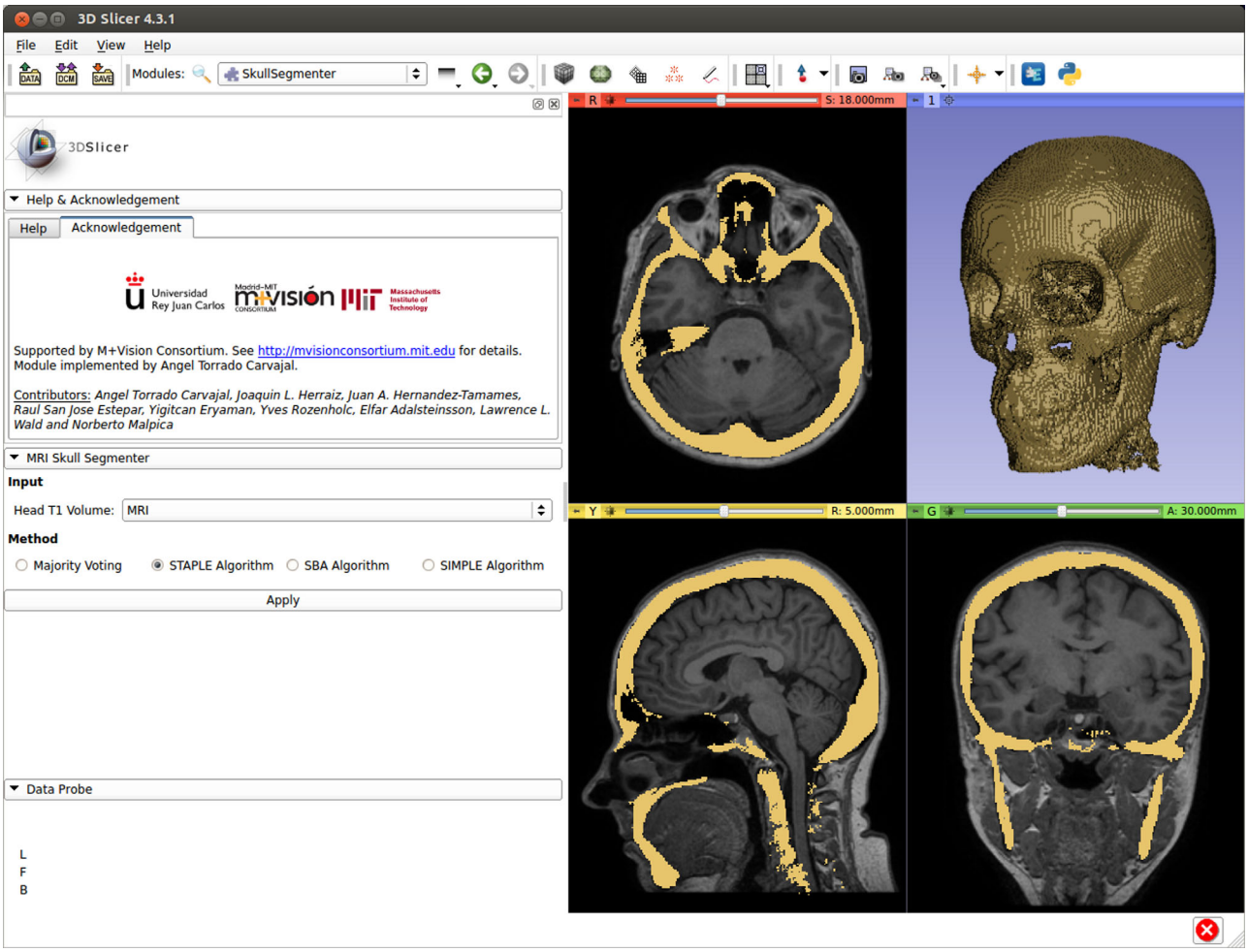

FIG. 3. Graphical user interface of the skull segmenter extension. It allows loading a new MRI volume and estimating the skull by one of the four label fusion methods used in this study.

Figure 4B shows the performance of the different label fusion methods over the clinical CT-MRI dataset. The Dice coefficient between the ground truth and the automated segmentation presents a value of $48.79 \pm 20.39\%$ for MV, $78.31 \pm 6.97\%$ for STAPLE, $73.70 \pm 7.24\%$ for SBA, and $58.06 \pm 7.80\%$ for SIMPLE.

Figure 4C shows the performance of the different label fusion methods on the whole head CT-MRI pair. The Dice coefficient between the ground truth and the automated segmentation presents a value of 77.67% for MV, 78.68% for STAPLE, 77.22% for SBA, and 77.67% for SIMPLE.

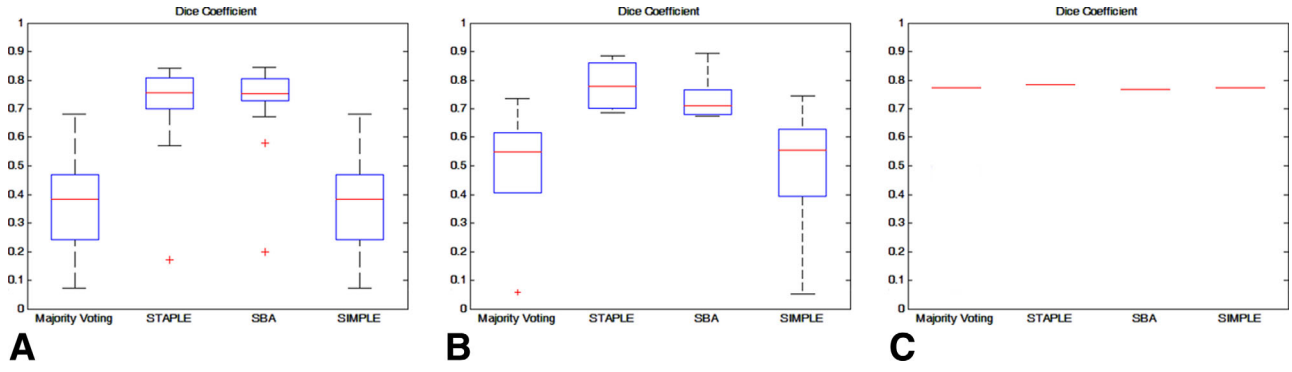

FIG. 4. Box and whisker plots of the Dice coefficient for the four estimation methods over the RIRE dataset (**A**), the clinical CT-MRI dataset (**B**), and the whole head CT-MRI pair (**C**). On each box, the central mark is the median, the edges of the box are the 25th and 75th percentiles, the whiskers extend to the most extreme data points [1.5 × inter-quartile range (IQR)], and outliers are plotted individually.

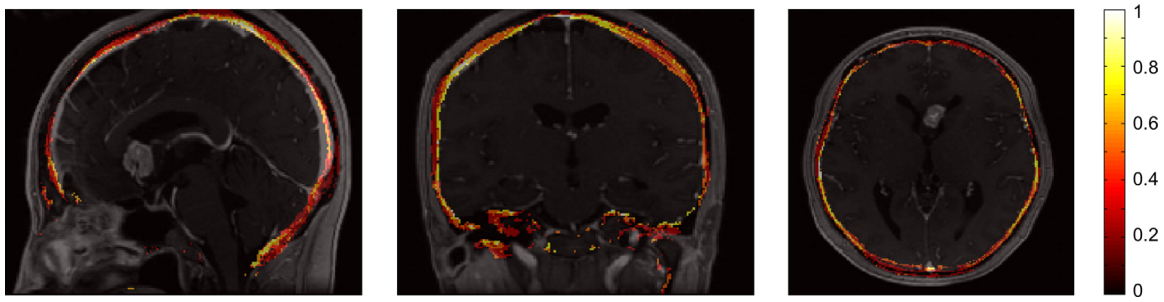

FIG. 5. Distribution of the segmentation fractional error for the STAPLE estimation approach over the clinical head CT-MRI pairs database. In this error map 0 represents that all subjects in the dataset were appropriately segmented in that voxel, while 1 represents all subjects were inaccurately segmented. A representative slice in each plane (sagittal, coronal and axial) is represented.

The DICE coefficient is a global measurement of segmentation quality. We have analyzed the spatial distribution of the fractional error by aligning all individual error masks to a template and computing the average error distribution, which is shown in Figure 5. Of the voxels showing some misclassification, only 2% showed a fractional error over 0.5 (the voxel was misclassified in more than half of the patients).

We have also measured the execution time for the three datasets. Table 1 shows the time taken by a complete execution of the registration and each label fusion approach on all datasets. The mean execution time and the 95% confidence interval are presented for each of the methods.

Qualitative Results

Visual inspection of the different approaches compared with the ground truth provides further assessment. Figure 6 shows the estimation result in five slices of a complete head MRI volume of a healthy subject. The method approaches the shape of the skull generally well. However, it can be seen that in some places, such as the frontal sinuses or cervical vertebrae, the estimation deviates from the ground truth skull contour.

Figure 7 shows the 3D rendering for 10 subjects. In this representation we can appreciate the level of detail of the approach.

The evaluation of our method on the RIRE dataset provides more information regarding the estimation of the skull on unhealthy subjects. Figure 8 shows the resulting mask in six pathological subjects from this dataset. The method is able to estimate the boundaries of the skull avoiding the pathological structures, even when they are close to the skull boundaries.

Table 1
Comparison of the Execution Time (Mean with 95% Confidence Interval) Taken in Estimating the Skull for All the Subjects in the Different Datasets Using the Four Label-Fusion Approaches for Each[a]

Dataset	Label fusion technique	Registration time (minutes)	Label fusion time (seconds)
RIRE	MV	19.50 ± 4.57	0.47 ± 0.09
	STAPLE		11.86 ± 2.17
	SBA		35.64 ± 5.16
	SIMPLE		15.50 ± 2.69
Clinical CT-MRI pairs	MV	22.89 ± 1.58	0.98 ± 0.10
	STAPLE		53.73 ± 3.47
	SBA		23.40 ± 1.47
	SIMPLE		21.56 ± 2.16
Head CT-MRI pair	MV	21.71 ± 2.22	1.83 ± 0.07
	STAPLE		38.88 ± 3.16
	SBA		84.30 ± 5.15
	SIMPLE		39.73 ± 1.29

[a]Registration time refers to the time taken in registering the whole dataset to the input image. We performed 20 executions for the CT-MRI pair to obtain the mean execution time, as this dataset only contained one subject.

DISCUSSION

MRI-based bone segmentation, and particularly automatic segmentation of the skull, is a challenging task. Due to the nature of the tissue properties, bone and air present low signal intensity on MR images, making it difficult to accurately delimit the bone boundaries, while the high complexity of the skull anatomy, its fuzzy boundaries and missing edge features make it difficult to apply general purpose segmentation methods.

The estimation of the skull based only on the patient-specific MRI is feasible with a previous CT atlas dataset and label fusion techniques. The results show how the estimation of the skull adjusts to the bone boundary limits while differentiating the air. The strategy of this method is to leverage the benefits of "a priori" knowledge from the CT atlas dataset and label fusion techniques.

The proposed method is able to approximate the skull contours and differentiate air from bone with similar accuracy as the results presented in Wang et al (11), that reported a Dice coefficient of 0.75, even though they only showed results on the upper half of the skull. Additionally, their method requires previous annotation of the database by an expert, while our method requires no previous manual intervention.

As a result of the label fusion volume averaging, the contours of the skull are smoothed in several places. For example, our method fails to capture the details of the bone spikes in the area inside the sinuses, as seen in Figure 5. However, these errors are not crucial in most of the potential applications of our method. The skull estimation presented in this study has been successfully used to create complete patient-specific tissue models

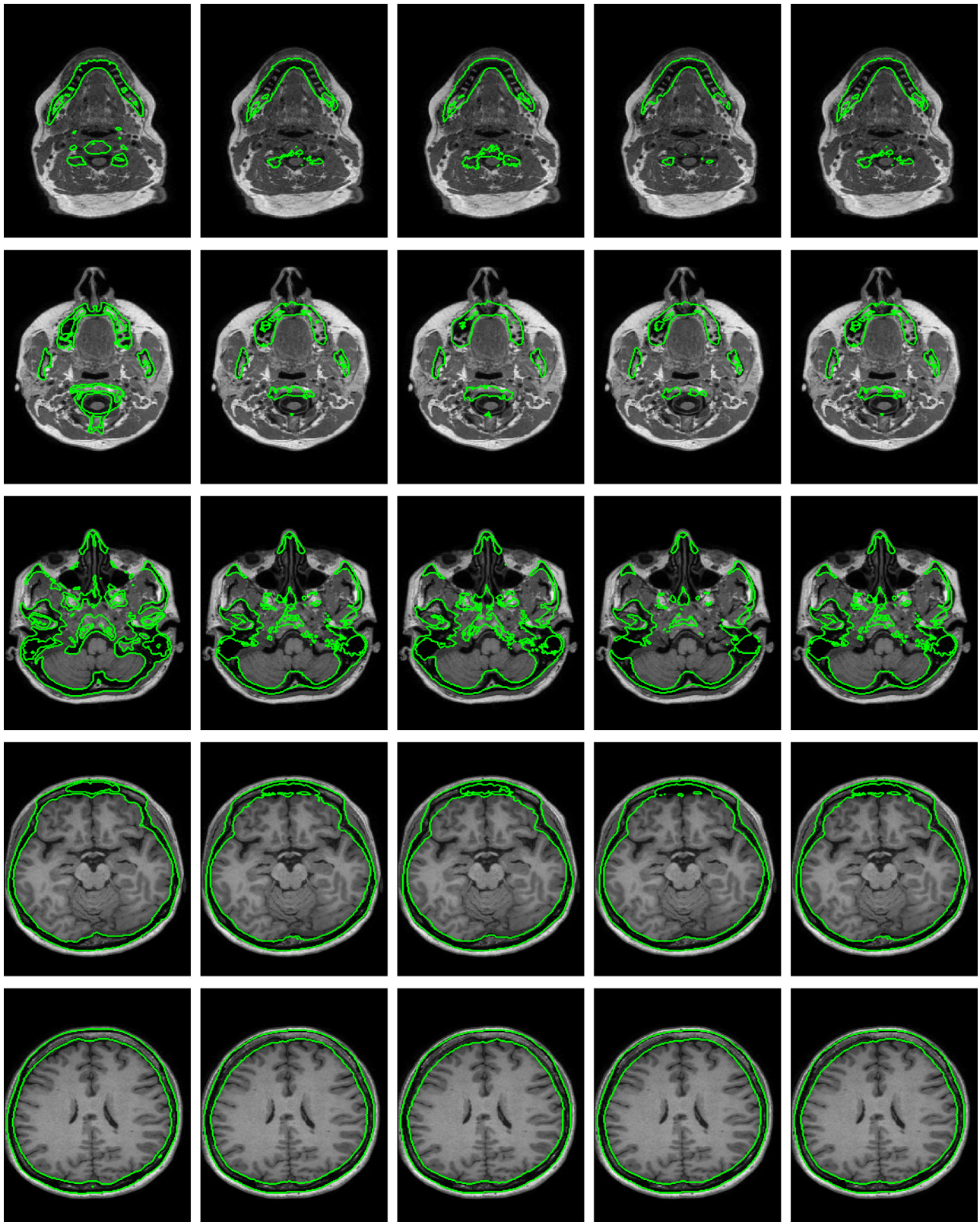

FIG. 6. Skull segmentation in five axial slices of an MRI volume. From left to right: CT ground truth segmentation, MV estimation, STAPLE estimation, SBA estimation, and SIMPLE estimation.

for EM modeling in EEG/MEG forward problem solving (36) and local SAR management (37,38), and PET/MR attenuation correction (39).

Our pipeline requires cross-modality registration, so that similarity based approaches to label-fusion are not directly applicable. Better results could be achieved

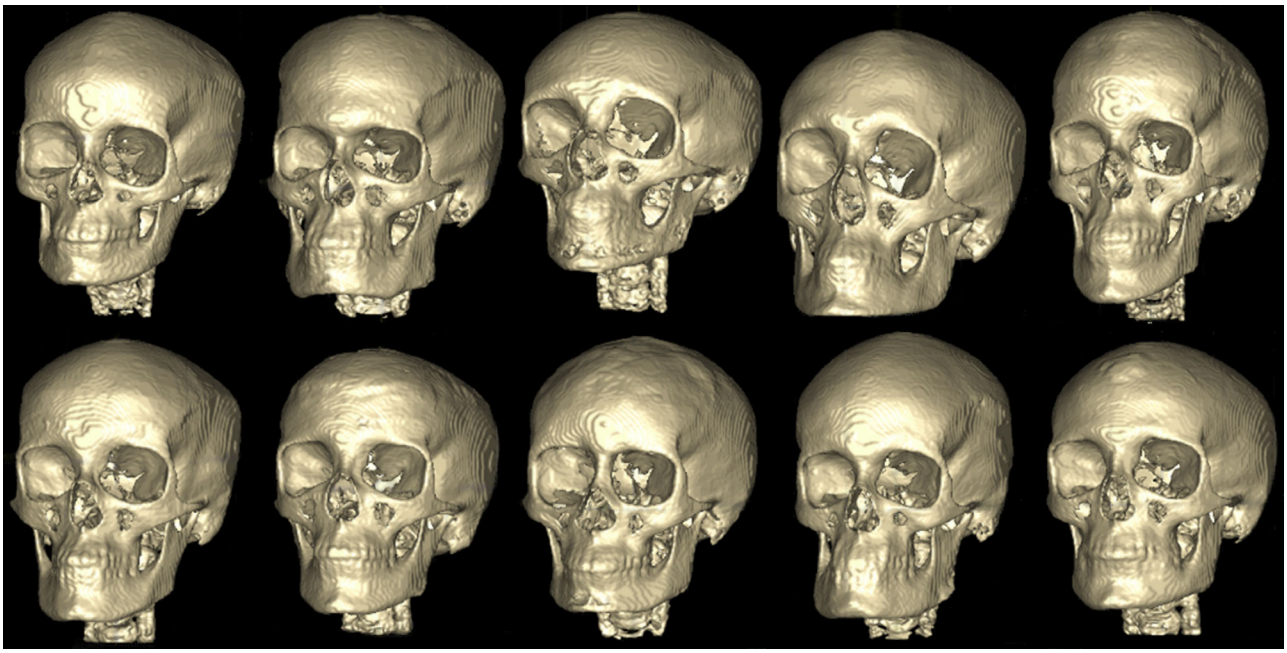

FIG. 7. Reconstruction of the skull for 10 subjects in the study. These segmentations were obtained using the STAPLE estimation approach.

using MRI-to-MRI registration, should we have MR-CT pairs for all subjects in the database.

Visual inspection of the segmentation results shows the high quality of the segmentations, and the robustness of the method in the presence of tumors and other brain pathologies. The use of this approach may lead to a decrease in patient ionization by removing the need of patient-specific CT acquisitions while obtaining a good estimation of the ground truth. These results are promising and may be included in several protocols such as brain studies in PET-MR scanners.

As can be seen in Table 1, the main drawback of the proposed method is the computational burden introduced by the multiple registrations and information fusion from the entire training data. Our approach provides good results, but computing many non-rigid

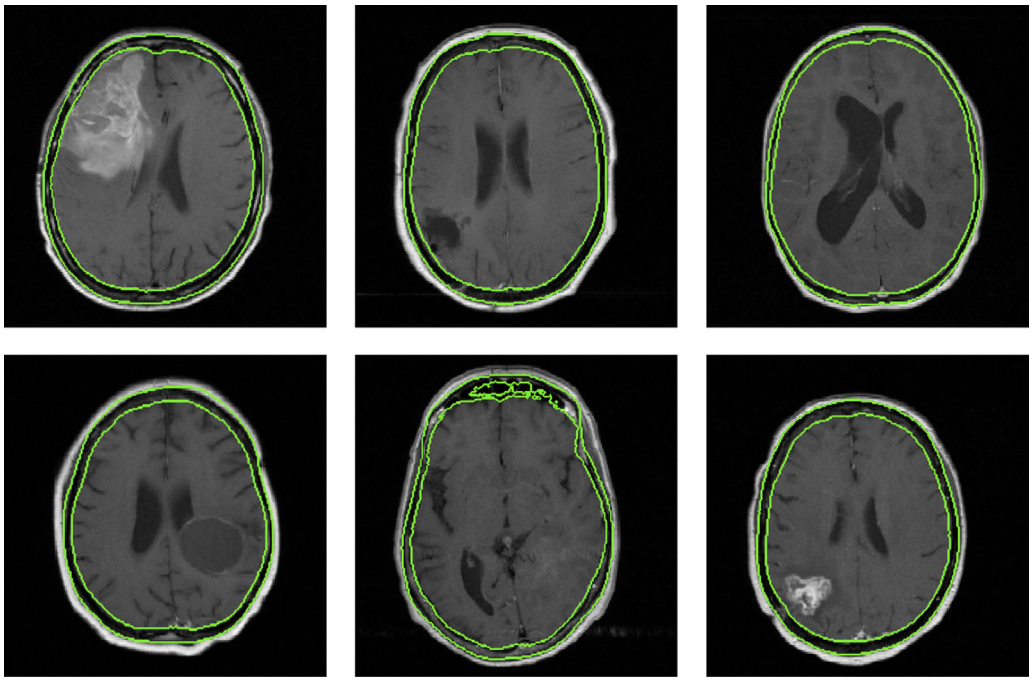

FIG. 8. Boundaries of the skull estimation method on patients presenting different neurological diseases. The skull estimation generalizes well, avoiding pathological tissues independently from their signal (hypoechoic or hyperechoic).

registrations is very time consuming. However, the gain to a patient by not perfoming a CT scan fully justifies the computational cost. Parallelization of the pipeline could reduce the overall time taken for skull estimation. Increasing the size and variety of the atlas could improve the accuracy of the results.

CONCLUSIONS

In this study, we have presented an approach for the estimation of the human skull by using a multi-atlas and label fusion approach based on acquired MR images only. The algorithm presented in this work removes the need of a patient-specific CT acquisition. The approach performs successfully on a wide range of data and could be useful for tasks where the skull estimation is needed such as PET/MR attenuation correction, and SAR calculations.

ACKNOWLEDGMENTS

The authors thank Dr. Juan Alvarez-Linera from Ruber International Hospital in Madrid for kindly providing the clinical datasets, and the anonymous reviewers for their valuable comments and suggestions that helped to improve the quality of the study.

REFERENCES

1. Hand JW. Modelling the interaction of electromagnetic fields (10 MHz–10 GHz) with the human body: methods and applications. Phys Med Biol 2008;53:R243.
2. Homann H, Graesslin I, Eggers H, Nehrke K, Vernickel P, Katscher U, Dössel O, Börnert P. Local SAR management by RF shimming: a simulation study with multiple human body models. MAGMA 2012;25:193–204.
3. Andreo P. Monte Carlo techniques in medical radiation physics. Phys Med Biol 1991;36:861.
4. Martinez-Möller A, Souvatzoglou M, Delso G, Bundschuh RA, Chefd'hotel C, Ziegler SI, Navab N, Schwaiger M, Nekolla SG. Tissue classification as a potential approach for attenuation correction in whole-body PET/MRI: evaluation with PET/CT data. J Nucl Med 2009;50:520–526.
5. Berker Y, Franke J, Salomon A, et al. MRI-based attenuation correction for hybrid PET/MRI systems: a 4-class tissue segmentation technique using a combined ultrashort-echo-time/Dixon MRI sequence. J Nucl Med 2012;53:796–804.
6. Wagenknecht G, Kaiser HJ, Mottaghy FM, Herzog H. MRI for attenuation correction in PET: methods and challenges. MAGMA 2013;26:99–113.
7. Jin J, Liu F, Weber E, Crozier S. Improving SAR estimations in MRI using subject-specific models. Phys Med Biol 2012;57:8153.
8. Akahn Z, Acar CE, Gencer NG. Development of realistic head models for electromagnetic source imaging of the human brain. In Proceedings of the 23rd Annual International Conference of the IEEE EMBS, Istanbul, Turkey, 2001. p 899–902.
9. Dogdas B, Shattuck DW, Leahy RM. Segmentation of skull and scalp in 3-D human MRI using mathematical morphology. Hum Brain Mapp 2005;26:273–285.
10. Rifai H, Bloch I, Hutchinson S, Wiart J, Garnero L. Segmentation of the skull in MRI volumes using deformable model and taking the partial volume effect into account. Med Image Anal 2000;4:219–233.
11. Wang D, Shi L, Chu WC, Cheng JC, Heng PA. Segmentation of human skull in MRI using statistical shape information from CT data. J Magn Reson Imaging 2009;30:490–498.
12. Robson MD, Bydder GM. Clinical ultrashort echo time imaging of bone and other connective tissues. NMR Biomed 2006;19:765–780.
13. Keereman V, Fierens Y, Broux T, De Deene, Y, Lonneux M, Vandenberghe S. MRI-based attenuation correction for PET/MRI using ultrashort echo time sequences. J Nucl Med 2010;51:812–818.
14. Berker Y, Franke J, Salomon A, et al. MRI-based attenuation correction for hybrid PET/MRI systems: a 4-class tissue segmentation technique using a combined ultrashort-echo-time/Dixon MRI sequence. J Nucl Med 2012;53:796–804.
15. Belardinelli P, Mastacchi A, Pizzella V, Romani GL. Applying a visual segmentation algorithm to brain structures MR images. In Proceedings of the 1st International IEEE EMBS Conference on Neural Engineering, Capri Island, Italy, 2003. p 507–510.
16. Hsu SH, Cao Y, Huang K, Feng M, Balter JM. Investigation of a method for generating synthetic CT models from MRI scans of the head and neck for radiation therapy. Phys Med Biol 2013;58:8419.
17. Torrado-Carvajal A, Hernandez-Tamames JA, Herraiz JL, Eryaman Y, Rozenholc Y, Adalsteinsson E, Wald LL, Malpica N. A multi-atlas and label fusion approach for patient-specific MRI based skull segmentation. In Proceedings of the 22nd Joint Annual Meeting ISMRM-ESMRMB, Milan, Italy, 2014. Abstract 1177.
18. Torrado-Carvajal A, Hernandez-Tamames JA, Herraiz JL, Eryaman Y, Adalsteinsson E, Wald LL, Malpica N. Automatic segmentation pipeline for patient-specific MRI tissue models. In Proceedings of the 22nd Joint Annual Meeting ISMRM-ESMRMB, Milan, Italy, 2014. Abstract 4906.
19. Lam L, Suen CY. Application of majority voting to pattern recognition: an analysis of its behavior and performance. IEEE Trans Syst Man Cybern A Syst Hum 1997;27:553–568.
20. Warfield SK, Zou KH, Wells WM. Simultaneous truth and performance level estimation (STAPLE): an algorithm for the validation of image segmentation. IEEE Trans Med Imaging 2004;23:903–921.
21. Rohlfing T, Maurer CR Jr. Shape-based averaging. IEE Trans Image Process 2007;16:153–161.
22. Langerak TR, van der Heide UA, Kotte AN, Viergever MA, van Vulpen M, Pluim JP. Label fusion in atlas-based segmentation using a selective and iterative method for performance level estimation (SIMPLE). IEEE Trans Med Imaging 2010;29:2000–2008.
23. Tilotta F, Richard F, Glaunès J, Berar M, Gey S, Verdeille S, Rozenholc Y, Gaudy JF. Construction and analysis of a head CT-scan database for craniofacial reconstruction. Forensic Sci Int 2009;191:112.e1–112.e2.
24. Collignon A, Maes F, Delaere D, Vandermeulen D, Suetens P, Marchal G. Automated multi-modality image registration based on information theory. Lect Notes Comput Sci 1995;3:263–274.
25. Viola P, Wells III WM. Alignment by maximization of mutual information. Int J Comput Vision 1997;24:137–154.
26. Maes F, Collignon A, Vandermeulen D, Marchal G, Suetens P. Multimodality image registration by maximization of mutual information. IEEE Trans Med Imaging 1997;16:187–198.
27. Pluim JP, Maintz JA, Viergever MA. Mutual-information-based registration of medical images: a survey. IEEE Trans Med Imaging 2003;22:986–1004.
28. Heckemann RA, Hajnal JV, Aljabar P, Rueckert D, Hammers A. Automatic anatomical brain MRI segmentation combining label propagation and decision fusion. Neuroimage 2006;33:115–126.
29. West J, Fitzpatrick JM, Wang MY, et al. Comparison and evaluation of retrospective intermodality brain image registration techniques. J Comput Assist Tomogr 1997;21:554–568.
30. The Retrospective Image Registration Evaluation Project, R.I.R.E. Version 2.0 Web site. http://www.insight-journal.org/rire/. Accessed March 2014.
31. Fedorov A, Beichel R, Kalpathy-Cramer J, et al. 3D Slicer as an image computing platform for the Quantitative Imaging Network. Magn Reson Imaging 2012;30:1323–1341.
32. Caban JJ, Joshi A, Nagy P. Rapid development of medical imaging tools with open-source libraries. J Digit Imaging 2007;20:83–93.
33. Kikinis R, Pieper SD, Vosburgh KG. 3D slicer: a platform for subject-specific image analysis, visualization, and clinical support. In: Jolesz FA, editor. Intraoperative imaging and image-guided therapy. New York: Springer; 2014. p 277–289.
34. Johnson H, Harris G, Williams K. BRAINSFit: mutual information rigid registrations of whole-brain 3D images, using the insight toolkit. Insight J 2007.
35. Dice LR. Measures of the amount of ecologic association between species. Ecology 1945;26:297–302.
36. Cuartas-Morales E, Torrado-Carvajal A, Hernandez-Tamames JA, Pineda JA, Manzanedo-Saenz E, Castellanos-Dominguez G. Influence of anisotropic blood vessels modeling in the EEG/MEG forward problem using MRI. In Proceedings of the 23rd Annual Meeting of ISMRM, Toronto, Canada, 2015.

37. Torrado-Carvajal A, Turk EA, Herraiz JL, Eryaman Y, Hernandez-Tamames JA, Adalsteinsson E, Wald LL, Malpica N. A comparison between three-point Dixon sequences and label fusion techniques for water-fat separation in high-field MRI local SAR estimation. In Proceedings of the 23rd Annual Meeting of ISMRM, Toronto, Canada, 2015.
38. Herraiz JL, Eryaman Y, Turk EA, et al. MRI planning for SAR management in pTx systems. In Proceedings of the 23rd Annual Meeting of ISMRM, Toronto, Canada, 2015.
39. Herraiz JL, Torrado-Carvajal A, Hernandez-Tamames JA, Malpica N. The effect of mouth motion on the attenuation correction in neurological PET studies. Lect Notes Comput Vision Biomech (in press).

SUPPORTING INFORMATION

Additional Supporting Information may be found in the online version of this article.